Modeling of Marangoni-Induced Droplet Motion and Melt Convection during Solidification of Hypermonotectic Alloys

MENGHUAI WU, ANDREAS LUDWIG, and LORENZ RATKE

A two-phase volume averaging approach to model Marangoni-induced droplet motion of the minority liquid phase and the convection in the parent melt during solidification of the hypermonotectic alloys is presented. The minority liquid phase decomposed from the parent melt as droplets in the miscibility gap was treated as the second-phase L_2. The parent melt including the solidified monotectic matrix was treated as the first phase L_1. Both phases were considered as different and spatially interpenetrating continua. The conservation equations of mass, momentum, solute, and enthalpy for both phases, and an additional transport equation for the droplet density, were solved. Nucleation of the L_2 droplets, diffusion-controlled growth, interphase interactions such as Marangoni force at the L_1-L_2 interface, Stokes force, solute partitioning, and heat release of decomposition were taken into account by corresponding source and exchange terms in the conservation equations. The monotectic reaction was modeled by adding the latent heat on the L_1 phase during monotectic reaction, and applying an enlarged viscosity to the solidified monotectic matrix. A two-dimensional (2-D) square casting with hypermonotectic composition (Al-10 wt pct Bi) was simulated. This paper focused on Marangoni motion, hence gravity was not included. Results with nucleation, droplet evolution, Marangoni-induced droplet motion, solute transport, and macrosegregation formation were obtained and discussed.

I. INTRODUCTION

ALLOYS with a miscibility gap in the liquid state, especially those with an alloy composition above the monotectic point (hypermonotectic), are potential bearing materials for the automotive industry, if the soft minority phase (normally in droplets) can be well dispersed in the hard matrix.[1,2] However, the spatial separation of the minority phase from the parent melt seems unavoidable regardless of whether the alloy solidifies under normal terrestrial conditions[3] or in a reduced gravity situation.[4,5] The reasons are sedimentation due to gravity and Marangoni (thermocapillary)-induced droplet motion. The former is easily understood, because the two liquid phases have generally a different density. The Marangoni-induced droplet motion is due to the temperature gradient established during solidification, which leads to the droplet moving from cold toward hot regions. The surface tension at the liquid-liquid interface decreases with temperature. Great efforts have been made[6,7,8] in the last few decades to understand Marangoni-induced droplet motion of single droplets. How to model Marangoni motion of multiple droplets in a macroscopic system, especially in the presence of a complicated solidification process, still remains an open subject.

Modeling of solidification and phase separation is part of a multiphase problem. A multiphase volume-averaging approach was developed by Beckermann's group.[9–15] Both the liquid and solidified phases were treated as spatially interpenetrating continua. The transport equations for both liquid and solid were solved simultaneously, permitting a rigorous description of the liquid convection and solid motion, mass transfer, solute partitioning at the liquid-solid interface, and many other microscopic phenomena. However, there are some difficulties when describing the grain morphology in the pioneering model.[16–17] Therefore, we have used a modified two-phase model focusing on the globular equiaxed solidification,[18,19,20] where the morphology of the solid phase could be simplified as spheres.

This article uses the modified two-phase volume averaging approach to model the Marangoni motion of the droplets in hypermonotectic solidification. The ideal spherical morphology of the second phase permits an adequate description of the droplet growth kinetics and the hydrodynamic behavior (drag force). A two-dimensional (2-D) square casting with alloy Al-10 wt pct Bi is simulated. Emphasis is placed on the Marangoni phenomenon, hence gravity is not considered in this article.

II. MODELING

A. *Phase Definition and Model Assumptions*

A typical phase diagram of a binary monotectic system with alloy elements A and B is shown in Figure 1. For most industrial alloys, the concentration c_0 lies between c_m and c_c. Above the critical temperature T_c, both components are completely miscible. Below T_c, two liquid phases (L_1, L_2) can coexist between two liquidus (binodal) in equilibrium. At T_m, monotectic reaction occurs, $L_1 \rightarrow S_A + L_2$. As the temperature further drops below T_f^B, the component B solidifies. Generally, there must be an eutectic reaction $L_2 \rightarrow S_A + S_B$ at a temperature below T_f^B. Most often, however, the eutectic is a degenerate one.

MENGHUAI WU, Dr.-Ing., and ANDREAS LUDWIG, Professor and Director, are with Simulation and Modeling of Metallurgical Processes, University of Leoben, A-8700 Leoben, Austria. Contact e-mail: menghuai.wu@notes.uni.leoben.ac.at LORENZ RATKE, Professor, is with the Institute for Space Simulation, German Aerospace Research Establishment DLR, D-51140 Cologne, Germany.

Manuscript submitted November 19, 2002.

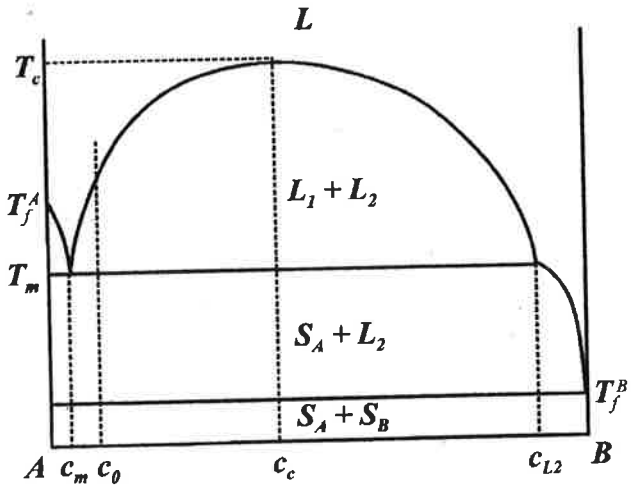

Fig. 1—Schematic phase diagram for systems with a liquid miscibility gap.

Normally there are four phases, L_1, L_2, S_A, and S_B, appearing in this system. The parent melt or the first liquid phase is considered as phase L_1. The second phase L_2 decomposes from L_1. Decomposition of L_2 from L_1 comprises the processes of nucleation and droplet growth. For simplicity, we further consider the first liquid phase and the solidified monotectic matrix ($S_A + L_2$) as the same phase L_1. The second liquid phase and its solidified counterpart are considered as the same phase L_2. With the monotectic reaction, the solidified monotectic matrix ($S_A + L_2$) is transformed directly from L_1. The hydrodynamic of the monotectic reaction is modeled in such a way that an artificially enlarged viscosity is given to the L_1 phase as it reaches the monotectic temperature. Additionally, the latent heat of the monotectic reaction is considered to be the L_1 phase. As L_2 droplets, which have formed during decomposition, approach the monotectic reaction front, they are modeled to be entrapped in the monotectic matrix by applying a similar artificially enlarged viscosity at and below the monotectic temperature. The solidification morphology of the monotectic itself is beyond the scope of this article. In addition to the preceding phase definition, the following assumptions are made in the recent model:

1. no gravity is considered;
2. there is no solidification shrinkage (it is assumed that $\rho_2 = \rho_1$);
3. both liquid phases have the same viscosity;
4. the eutectic reaction of L_2 is ignored;
5. there is no collision and coalescence (coagulation) of droplets; and
6. diffusion in a single droplet is infinite.

B. *Conservation Equations*

The conservation equation, together with source terms, exchange (or transfer) terms, and some auxiliary terms, is listed in Table I. Both L_1 and L_2 phases transport according to the momentum conservation Eq. [2]. Decomposition (or dissolution) of L_2 is taken into account through a mass transfer term $M_{12}(= -M_{21})$, which is defined in Eq. [8]. Details about M_{12} (kg/m^3/s) are described in Section II–D. The volume fractions of both phases are subject to $f_1 + f_2 = 1$.

In the momentum conservation Eq. [2], the same viscosity for both phases is applied. Above T_m, the viscosity is taken as the viscosity of the parent melt μ_1, while when the monotectic reaction is finished, a large viscocity ($10^7 \cdot \mu_1$) is applied. Monotectic reaction takes place normally in a temperature range, depending on the particular alloy components. In this work, an empirical temperature range of 10 K is assumed. This range indicates that the liquid-solid transition starts at T_m and ends at $T_m - 10$. Therefore, the viscosity of phase L_1 is treated with a linear function to increase from μ_1 at T_m to the maximum $10^7 \cdot \mu_1$ at $T_m - 10$. The momentum exchange $\mathbf{U}_{12}$ $(= -\mathbf{U}_{21})$ in the momentum conservation equations includes two parts: one due to mass transfer $\mathbf{U}_{12}^p$ and one due to hydrodynamic forces (or Stokes forces) $\mathbf{U}_{12}^d$. Both terms are given in Eq. [9]. In order to define $\mathbf{U}_{12}^p$, two situations must be considered: decomposition and dissolution of the droplets. For decomposition, the momentum transferred from L_1 to L_2 is determined by the velocity of melt $\mathbf{u}_1$ and the mass-transfer rate M_{12}, hence $\mathbf{U}_{12}^p = \mathbf{u}^* \cdot M_{12}$ with $\mathbf{u}^* = \mathbf{u}_1$. By analogy, we have $\mathbf{U}_{12}^p = \mathbf{u}^* \cdot M_{12}$ with $\mathbf{u}^* = \mathbf{u}_2$ for dissolution. The hydrodynamic force $\mathbf{U}_{12}^d$ and the Marangoni force $\mathbf{F}_M$ are described in Section II–E.

The volume-averaged solute concentrations c_1 and c_2 are obtained by solving the species conservation Eq. [3]. The solute exchange $C_{12}(= -C_{21})$ at the L_1-L_2 interface includes also two parts: the solute partitioning due to phase change, C_{12}^p, and the species transfer at the L_1-L_2 interface C_{12}^d due to atom thermal motion. Here, the term C_{12}^d is neglected. For the solute partitioning C_{12}^p due to phase change, two situations are separately considered: decomposition and dissolution. With decomposition, the species transformed from L_1 to L_2 when ignoring the solute partitioning should be $c_1 \cdot M_{12}$. However, due to partitioning, the L_2 needs the amount of species $k \cdot c_1 \cdot M_{12}$, where $k > 1$. More solute element $(k - 1) \cdot c_1 \cdot M_{12}$ must be drawn from L_1. Therefore, we have $C_{12}^p = c^* \cdot M_{12}$ with $c^* = k \cdot c_1$ for decomposition in Eq. [10]. During dissolution, the solute transformed from L_2 to L_1 is $c_2 \cdot M_{21}$. This time the solute is completely accepted by L_1. Therefore, we have $C_{21}^p = c^* \cdot M_{21}$ with $c^* = c_2$ for dissolution in Eq. [10]. Additionally, in order to predict macrosegregation, a mixture concentration is defined with Eq. [12].

The enthalpy conservation Eq. [4] is solved separately for both phases. The exchange term $Q_{12}(= -Q_{21})$ is defined in Eq. [11]. It includes two parts: the part due to phase change Q_{12}^p and the part due to the L_1-L_2 interface heat transfer Q_{12}^d. In the present model, thermal equilibrium is assumed, *i.e.*, $T_1 = T_2$. To ensure this equilibrium numerically, the volume heat-transfer coefficient H^* in the enthalpy transfer term $Q_{12}^d = H^* (T_1 - T_2)$ should be chosen as large as possible. A too large H^*, however, will overwhelm the contribution of other terms in the energy conservation, and cause the divergence of the numerical calculation. In this study, test simulations are carried out, and a suitable large value for H^* (10^9 W/m^3/K) is obtained. With this quantity, the precondition of thermal equilibrium is maintained, and numerical calculation results are stable. To handle the term Q_{12}^p, decomposition and dissolution are considered separately. Please notice the definition of h_1 and h_2 in Eq. [4]; the enthalpy difference between two liquid phases $(h_1 - h_2)$ defines the decomposition heat Δh_d. During decomposition, the energy given by the L_1 phase is $Q_{12}^p = h_1 \cdot M_{12}$,

Table 1. Conservation Equations, Source, and Exchange (Transfer) Terms and Auxiliary Equations for the Numerical Model of Hypermonotectic Solidification

Conservation equations		
Mass:	$\frac{\partial}{\partial t}(f_1\rho_1) + \nabla\cdot(f_1\rho_1\mathbf{u}_1) = M_{21}$	
	$\frac{\partial}{\partial t}(f_2\rho_2) + \nabla\cdot(f_2\rho_2\mathbf{u}_2) = M_{12}$	[1]
Momentum:	$\frac{\partial}{\partial t}(f_1\rho_1\mathbf{u}_1) + \nabla\cdot(f_1\rho_1\mathbf{u}_1\otimes\mathbf{u}_1) = -f_1\nabla p + \nabla\cdot\bar{\bar{\tau}}_1 + f_1\rho_1\mathbf{g} + \mathbf{U}_{21} - \mathbf{F}_M$	
	$\frac{\partial}{\partial t}(f_2\rho_2\mathbf{u}_2) + \nabla\cdot(f_2\rho_2\mathbf{u}_2\otimes\mathbf{u}_2) = -f_2\nabla p + \nabla\cdot\bar{\bar{\tau}}_2 + f_2\rho_2\mathbf{g} + \mathbf{U}_{12} + \mathbf{F}_M$	
	where $\bar{\bar{\tau}}_1 = \mu_1 f_1(\nabla\otimes\mathbf{u}_1 + (\nabla\otimes\mathbf{u}_1)^T)$ and $\bar{\bar{\tau}}_2 = \mu_2 f_2(\nabla\otimes\mathbf{u}_2 + (\nabla\otimes\mathbf{u}_2)^T)$	[2]
Species:	$\frac{\partial}{\partial t}(f_1\rho_1 c_1) + \nabla\cdot(f_1\rho_1\mathbf{u}_1 c_1) = \nabla\cdot(f_1\rho_1 D_1\nabla c_1) + C_{21}$	
	$\frac{\partial}{\partial t}(f_2\rho_2 c_2) + \nabla\cdot(f_2\rho_2\mathbf{u}_2 c_2) = \nabla\cdot(f_2\rho_2 D_2\nabla c_2) + C_{12}$	[3]
Enthalpy:	$\frac{\partial}{\partial t}(f_1\rho_1 h_1) + \nabla\cdot(f_1\rho_1\mathbf{u}_1 h_1) = \nabla\cdot(f_1 k_1\nabla\cdot T_1) + Q_{21} + \Delta h_M$	
	$\frac{\partial}{\partial t}(f_2\rho_2 h_2) + \nabla\cdot(f_2\rho_2\mathbf{u}_2 h_2) = \nabla\cdot(f_2 k_2\nabla\cdot T_2) + Q_{12}$	
	where $h_1 = \int_{T_{ref}}^{T_1} c_{p(1)}dT + h_1^{ref}$ and $h_2 = \int_{T_{ref}}^{T_2} c_{p(2)}dT + h_2^{ref}$	[4]
Droplet density:	$\frac{\partial}{\partial t}n + \nabla\cdot(\mathbf{u}_2 n) = N$	[5]
Source terms:		
Nucleation:	$N = \frac{d\Delta T}{dt}\cdot\frac{n_{max}}{\sqrt{2\pi}\cdot\Delta T_\sigma}\cdot e^{-\frac{1}{2}\left(\frac{\Delta T-\Delta T_N}{\Delta T_\sigma}\right)^2}$	[6]
Marangoni force:	$\mathbf{F}_M = \frac{6}{(1+\mu_2/\mu_1)\cdot(2+k_2/k_1)}\cdot\frac{f_2}{d_2}\cdot\frac{\partial\sigma}{\partial T}\cdot\nabla T$	[7]
Exchange (transfer) terms		
Mass transfer	$M_{12} = n\cdot\pi d_2\cdot\rho_2\cdot\frac{D_1}{\Delta c_d}\cdot\Delta c\cdot f_1$	[8]
Momentum:	$\mathbf{U}_{12} = \mathbf{U}_{12}^d + \mathbf{U}_{12}^p \quad \mathbf{U}_{12}^p = \mathbf{u}^*\cdot M_{12} \quad \mathbf{U}_{12}^d = K_{12}(\mathbf{u}_1 - \mathbf{u}_2)$	[9]
Species:	$C_{12} = C_{12}^d + C_{12}^p \quad C_{12}^p = c^*\cdot M_{12} \quad C_{12}^d$ neglected	[10]
Enthalpy:	$Q_{12} = Q_{12}^d + Q_{12}^p \quad Q_{12}^p = h^*\cdot M_{12} \quad Q_{12}^d = H^*\cdot(T_1 - T_2)$	[11]
Auxiliary terms		
Mix concentration:	$c_{mix} = \frac{c_1\cdot\rho_1\cdot f_1 + c_2\cdot\rho_2\cdot f_2}{\rho_1\cdot f_1 + \rho_2\cdot f_2}$	[12]
Droplet diameter:	$f_2 = \frac{\pi d_2^3}{6}\cdot n$	[13]

from which, however, only the amount of $h_2 \cdot M_{12}$ is added to the L_2 phase. The energy difference $(h_1 - h_2) \cdot M_{12}$, *i.e.*, the energy release due to decomposition, will be left to L_1 phase. Referring to Eq. [11], we have $Q_{12}^p = h^* \cdot M_{12}$ with $h^* = h_2$. This manipulation would violate the thermal equilibrium precondition $T_1 = T_2$. With the volume heat transfer between both phases, the difference of T_1 and T_2 is leveled out immediately. By analogy, we have $Q_{12}^p = h^* \cdot M_{21}$ with $h^* = h_1$ for dissolution.

The keys for the enthalpy are the treatment of the decomposition heat Δh_d and the latent heat of monotectic reaction Δh_M. The value of Δh_d is considered in the numerical model by the enthalpy difference $(h_1 - h_2)$.[18] Care must be taken when choosing T_{ref}, h_1^{ref}, and h_2^{ref} in Eq. [4], so as to maintain $h_1 - h_2 = \Delta h_d$. The value of Δh_d is determined from the thermodynamic calculation.[21] It is normally composition dependent, but here, a constant value referring to the concentration c_0 is taken. The latent heat of monotectic reaction Δh_M is applied on the L_1 phase. As assumed previously, the monotectic reaction takes place in an empirical temperature range 10 K. Correspondingly, the latent heat is treated to release in a piecewise linear manner in the given temperature range. The value of Δh_M is determined from the latent heat of pure component A multiplied by a factor of mass fraction A $(1 - c_m/C_{12})$ according to the lever rule (Figure 1).

The conservation of droplet density n is formulated in Eq. [5]; n is transported according to the velocity of L_2. The source term N, namely, nucleation rate of the droplets, is defined in Eq. [6], and described in Section C.

C. *Nucleation and Droplet Transport*

A heterogeneous nucleation law, which was previously applied for globular equiaxed solidification, is here employed for the nucleation of L_2 droplet.[18,20,22,23] This approach is based on the assumption that there exist many potential nucleation sites in the parent melt. The nucleation sites belong to different families. Each family can only be activated as newly nucleated droplets when a corresponding undercooling ΔT is achieved. The ΔT serves as the driving force for the nucleation. The statistical outcome of all the families of the nucleation sites is described with a Gaussian distribution:

$$\frac{dn}{d\Delta T} = \frac{n_{\max}}{\sqrt{2\pi}\cdot\Delta T_\sigma}\cdot e^{-\frac{1}{2}\left(\frac{\Delta T-\Delta T_N}{\Delta T_\sigma}\right)^2} \qquad [14]$$

where the parameters $n_{\max}$, ΔT_N, and ΔT_σ are determined experimentally.[23]

The potential nucleation sites are assumed to be stationary. Only the nucleated droplets are allowed to move according to $\mathbf{u}_2$. Taking a volume element as an example, the potential sites within this volume element are previously assigned. As a ΔT is achieved, a certain amount of droplets are nucleated correspondingly. The sites from which the droplets have already nucleated are exhausted from the volume element. The remaining nucleation sites can only be activated with a larger ΔT. The maximum undercooling ever achieved for the considered volume element is recorded as $\Delta T_{\max}$. If the actual ΔT is smaller than $\Delta T_{\max}$, no further droplet nucleates. When the actual ΔT is larger than $\Delta T_{\max}$, new droplets nucleate, and the $\Delta T_{\max}$ is updated with the actual ΔT, and so on. Whether nucleated droplets remain in this volume element or move to the neighbor elements does not influence the preceding nucleation procedure. In the case of dissolution (droplets are exposed to the overheated zone), the nucleation rate is set to zero until the volume fraction of L_2 reduces below 0.01 pct. Then a dissolution rate is calculated in a way similar to the preceding description.

In order to implement the nucleation law, N in Eq. [5] is defined as $[dn/d(\Delta T)]\cdot[d(\Delta T)/dt]$. Because nucleation occurs in a partially decomposed volume element, an Avrami factor f_1 is necessarily considered in Eq. [6].

D. *Droplet Growth and Mass Transfer*

Growth speed of L_2 droplets depends on the species diffusion in the parent melt. The problem of diffusion-controlled growth of a precipitate in a supersaturated matrix was analytically solved as early as 1949 by Zener.[1,21] Here, it is employed to model the growth of the droplets.

As a droplet grows, a special concentration profile around the droplet is established (Figure 2). The far-field concentration in L_1 is c_1, which is determined by Eq. [3]. It is assumed that the local thermodynamic equilibrium always holds at the L_1-L_2 interface. The concentration in L_1 at the interface can be determined from phase diagram c_1^* corresponding to temperature T. In the case of $k > 1$, the far-field concentration c_1 is higher than the equilibrium concentration c_1^* at the interface. The diffusion of solute element B from far field to the interface plays the dominant role in the droplet growing process. Solution to the diffusion-controlled growth is expressed as

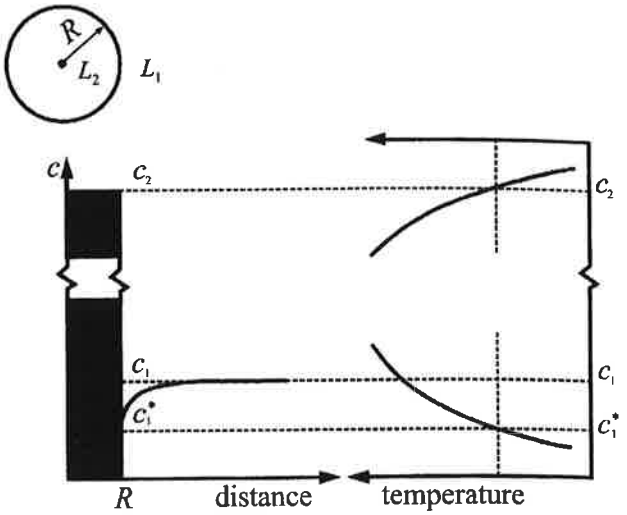

Fig. 2—Schematic of the concentration profile ahead of a growing droplet with respect to the binodal in the phase diagram.

$$\frac{dR}{dt} = \frac{D_1}{d_2}\cdot\frac{\Delta c}{\Delta c_d} \qquad [15]$$

where $\Delta c = c_1 - c_1^*$ and $\Delta c_d = c_2^* - c_1^* \approx c_2 - c_1^*$; d_2 is the diameter of the L_2 droplet. For the most used monotectic alloys, the decomposed second phase has the composition near the pure component B. The diffusion in a single droplet is assumed to be infinite, *i.e.*, $c_2^* = c_2$. From Eq. [15], the mass-transfer rate for a single droplet m_{12} (kg/s) can be modeled as

$$m_{12} = \pi d_2\cdot\rho\cdot\frac{D_1}{\Delta c_d}\cdot\Delta c \qquad [16]$$

When the droplet density n and an additional Avrami factor f_1 are considered, the mass-transfer rate per volume M_{12} (kg/m^3/s) is defined in Eq. [8].

E. *Marangoni Force and Hydrodynamic Resistance*

As a droplet is placed in the melt with a temperature gradient ∇T, thermocapillary convections in or around the droplet are induced (Figure 3). The droplet surface is drawn from hotter pole towards the colder pole in order to lower the surface tension. Consequently the droplet moves towards hot region. It is called Marangoni induced droplet motion, or simply Marangoni motion. Marangoni force $\mathbf{f}_M$ is defined by integration of the thermocapillary force acting on the droplet surface. On a droplet with a relative velocity $\Delta\mathbf{u}$ respecting to the matrix, a hydrodynamic resistance, called Stokes force $\mathbf{f}_{st}$, exists. Based on Stokes–Rybczynski–Hadamard approximation, Young *et al.*[6] Gunter[7] and Velarde[8] have deduced $\mathbf{f}_M$ and $\mathbf{f}_{st}$ for single droplets.

$$\mathbf{f}_M = \frac{\pi d_2^2}{(1+\mu_2/\mu_1)\cdot(2+k_2/k_1)}\cdot\frac{\partial\sigma}{\partial T}\cdot\nabla T \qquad [17]$$

Further considering the droplet density n and the relation of Eq. [13], the volume-averaged Marangoni force $\mathbf{F}_M$ (N/m^3), which is required for the macro momentum conservation equations, is obtained (Eq. [7]). The key parameter to model the Marangoni motion is $\partial\sigma/\partial T$, named the "Marangoni coefficient." Many experimental studies were carried out in the last decades on the surface tension for monotectic alloys. A general relationship is recommended by[1,21,24]

$$\sigma = \sigma_0 \cdot \left(1 - T/T_c\right)^{1.26} \qquad [18]$$

or

$$\frac{\partial \sigma}{\partial T} = -1.26 \cdot \sigma_0 \cdot \frac{1}{T_c} \cdot \left(1 - T/T_c\right)^{0.26} \qquad [19]$$

where σ_0 is determined experimentally.

The Stokes force for a single droplet is

$$\mathbf{f}_{st} = 2\pi d_2 \cdot \mu_1 \cdot \frac{1 + 3\mu_2/2\mu_1}{1 + \mu_2/\mu_1} \cdot \Delta\mathbf{u} \qquad [20]$$

From Eq. [20], the volume-averaged parameter K_{12} in Eq. [9] is deduced.

$$K_{12} = \frac{1 + 3\mu_2/2\mu_1}{1 + \mu_2/\mu_1} \cdot \frac{12 f_2}{d_2^2} \cdot \mu_1 \qquad [21]$$

F. *Numerical Implementation*

The conservation equations, Eqs. [1] through [5] are numerically solved by using the fully implicit, control-volume-based CFD software FLUENT version 4.5.6.*

*FLUENT is a trademark of Fluent, Inc., USA.

A single pressure field p is shared by both phases. The pressure correction equation is obtained from the sum of the normalized mass continuity equations, Eq. [1]. It is solved by using an extended SIMPLE algorithm.[25] For each time-step, up to 60 iterations were necessarily made to decrease the normalized residual of c_1, c_2, f_2, $\mathbf{u}_1$, $\mathbf{u}_2$, p, and n below the convergence limit of 10^{-4} and h_1 and h_2 below 10^{-6}. In each iteration, the auxiliary droplet diameter d_2 is updated first. Then, the exchange/transfer terms U_{12}, C_{12}, and Q_{12}, and the source terms N and M_{12}, are calculated based on the variables obtained in the last iteration. Finally, the conservation equations of momentum, mass, enthalpy, and species are solved.

Theoretically, there is no stability criterion that needs to be met to determine Δt because FLUENT formulation is fully implicit. However, the time-steps used impact the accuracy, and hence the reliability, of the numerical results. Due to the complexity of the coupling, there is no formulation to determine the optimal Δt. It must be determined empirically by test simulations. In the program, an automatic Δt controller is integrated.[18] An initial time-step is given. If more than 40 iterations for each time-step are needed to meet the convergence criterion, the program reduces Δt. If in less than 20 iterations convergence is met, then a larger Δt is used.

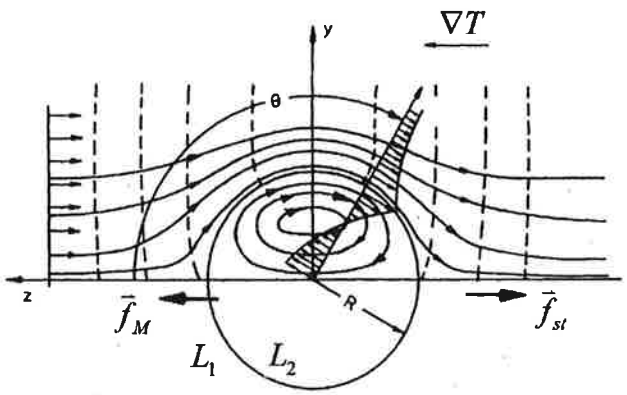

Fig. 3—Thermocapillary convection in and around the droplet. Referring to the droplet, the Marangoni force $\mathbf{f}_M$ drives the droplet to move in the ∇T direction, and the hydrodynamic resistance (or Stokes force) $\mathbf{f}_{st}$ points to the reverse direction of the droplet motion.

III. PROBLEM DESCRIPTION

A 2-D square casting (90 × 90 mm^2) with the composition Al-10 wt pct Bi is simulated. The calculation domain is meshed into 20 × 20 square volume elements. The size of each element is 5 × 5 mm^2. The finer the volume elements are, the smaller the time-step Δt needed to meet the convergence criterion, and hence the higher the computation cost. In the simulations presented subsequently, the automatic time-step controller[18] is activated. The smallest time-step reached during calculation is $\Delta t = 1 \times 10^{-4}$ s. A single run of the simulation took 2 weeks on a SGI Octane R12000 workstation (Silicon Graphics GmbH, Grasbrunn, Germany).

The casting is considered to be filled instantaneously and to solidify under the condition without gravity. The initial temperature of the melt is 1065 K. The mold remains at a constant temperature of 290 K. The heat exchange coefficient H at the casting-mold interface is given as 750 W/(m^2·K).

Phase diagram parameters of the hypermonotectic alloy Al-10 wt pct Bi and its physical properties are listed in Tables II and III. The parameters used for the nucleation law in Eq. [6] are $n_{max} = 10^{13}$ m^{-3}, $\Delta T_N = 20$ K, and $\Delta T_\sigma = 8$ K. The casting solidifies in an enclosed system. In this work, we do not consider the feeding flow, which is caused by solidification shrinkage. The densities of the two liquid phases are taken as equal, *i.e.*, the value of ρ_1. To estimate the mass-transfer rate M_{12}, an initial grain diameter d_2 must be known. We assumed an initial droplet diameter of $d_2 = 1$ μm.

Table II. Notation of Phase Diagram Information of the Al-Bi System

Monotectic temperature	T_m	930 K	657 °C
Monotectic concentration	c_m	0.47 at. pct	3.526 wt pct
L_2 monotectic concentration	c_{L2}	83.4 at. pct	97.493 wt pct
Critical temperature	T_c	1310 K	1037 °C
Melting point of Al	T_f^A	933 K	660 °C
Melting point of Bi	T_f^B	543 K	270 °C
Gross concentration	c_0	1.415 at. pct	10 wt pct
Slope of liquidus at c_0	m	148.1 K/at. pct	20.42 °C/wt pct
Partitioning coefficient	k	51.72	9.55

IV. RESULTS AND DISCUSSION

The solidification sequence 3.6, 15.6, and 32.6 seconds after the start of cooling is shown in Figures 4 through 6, and the final prediction of f_s, c_{mix}, n, and d_2 in Figure 7. The velocity fields are shown by arrows. The scalar quantities are shown in gray scale together with isolines, and the corresponding value for each isoline is given. Some isolines show enclosed regions, which are marked with a value followed by "+" or "−," indicating that the quantity in the enclosed region is larger (+) or smaller (−) than the value given. Additionally, the monotectic front is also shown, and overlapped with the velocity field. As described in Section II-A, the monotectic reaction ($L_1 \rightarrow S_A + L_2$) occurs in a temperature range from 930 to 920 K. The monotectic front is defined here with the isotherm of $T = 925$ K. In front of the monotectic front droplet, motion and melt convection are observed, and behind the monotectic front, the reaction product (monotectic matrix) becomes rigid and the decomposed L_2 droplets during decomposition are entrapped in the monotectic matrix.

Table III. Thermophysical Properties Used for the Simulation[21,24,26]

$\rho_1 =$ 2340 kg/m	$c_{p(2)} =$ 124.8 J/kg/K	$\Delta h_d = 10.775$ kJ/kg
$k_1 =$ 238 W/m/K	$\mu_1 \approx \mu_2 =$ $1.03 \cdot 10^{-3}$ kg/m/s	$\Delta h_M = 383$ kJ/kg
$k_2 =$ 15.5 W/m/K	$D_1 =$ $1.1 \cdot 10^{-8}$ m²/s	$\sigma_0 = 0.1427$ J/m²
$c_{p(1)} =$ 917 J/kg/K	$D_2 = \infty$	

A. *Solidification Sequence and Phase Separation*

With the start of cooling, the temperature in the corners drops immediately below the binodal (1062.2 K for alloy 10 wt pct Bi), and the melt is undercooled. In 3.6 seconds (Figure 4), the droplets of Bi-enriched second phase L_2 nucleate there, and decomposition and growth start. The thermocapillary (Marangoni) force drives the droplets to move from the cold toward the hot region. As shown in the velocity field, the L_2 phase moves from the corners toward the casting center. In the meantime, the parent melt L_1 moves in the opposite direction, because the space of the leaving phase L_2 must be filled by the parent melt L_1. From Eq. [17], Marangoni force is governed by the temperature gradient ∇T. In the initial stage, the highest ∇T coincides with the highest droplet velocity. Marangoni-induced droplet motion leads to phase separation, *i.e.*, the droplet motion from the corners toward the casting center results in depletion of the L_2 phase f_2 in the corners and enrichment of the L_2 phase in the casting center. However, in the very initial stage, this phenomenon is not obviously seen. As shown in Figure 4(e), the corner regions have high f_2, while the f_2 values in other regions are lower. It implies that the decomposition, *i.e.*, the nucleation and the droplet growth, dominates in the initial stage. Where the undercooling is higher, there is higher nucleation and growth rate. The outcome of the phase separation in terms of the Marangoni-induced droplet motion can only be significant later. It is also noticed that the temperature of the entire casting in the initial 3.6 seconds is still above the monotectic point T_m; no monotectic reaction occurs.

Monotectic reaction occurs first in the corners, about 6 seconds after the cooling starts. The position of the monotectic front at 15.6 seconds is shown in Figures 5(c) and (d). With the monotectic reaction, a large amount of latent heat is

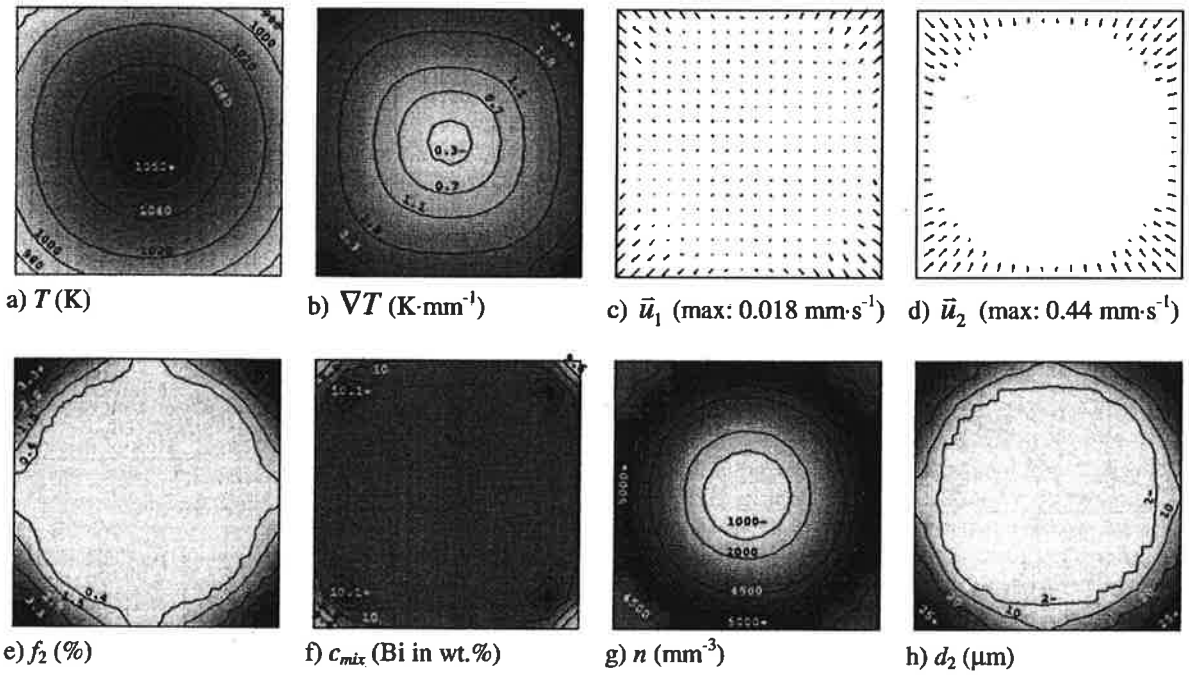

Fig. 4—(*a*) through (*h*) Simulation results at 3.6 s. The arrows of both velocities are linearly scaled from zero to the maximum value given. All other scalar quantities are shown with isolines together with 30 gray levels, with dark showing the highest value and bright the lowest.

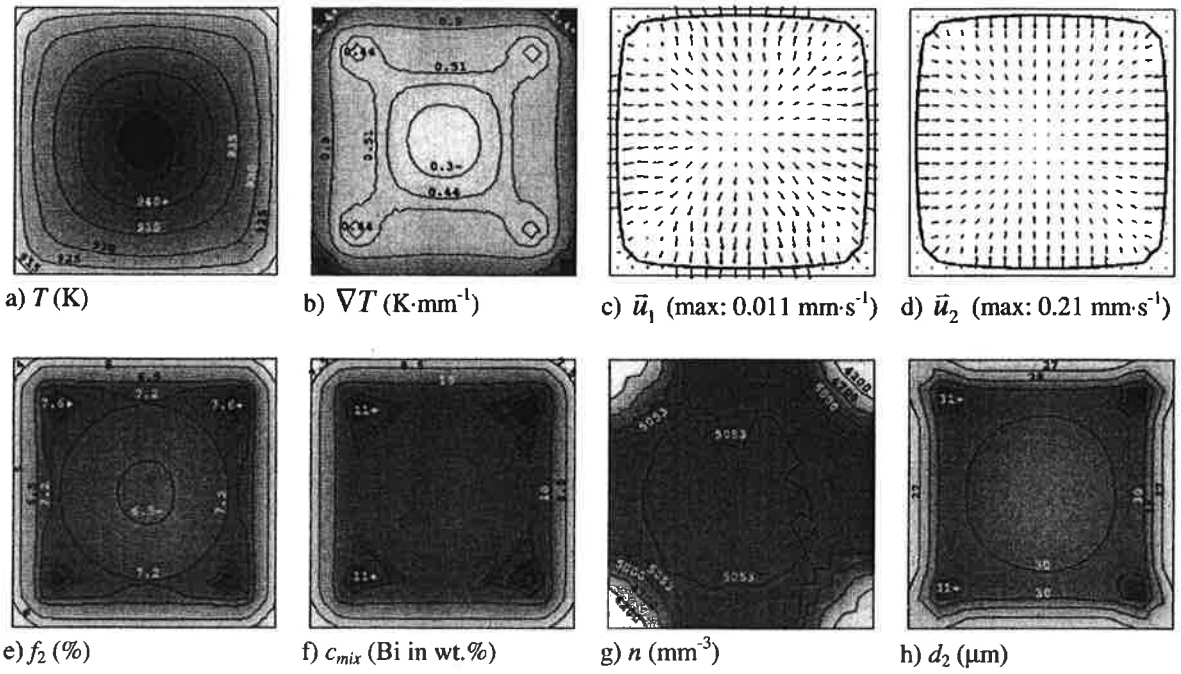

Fig. 5—(*a*) through (*h*) Simulation results at 15.6 s. The arrows of both velocities are linearly scaled from zero to the maximum value given, and the monotectic front (T = 925 K) is drawn together with the velocity fields. All other scalar quantities are shown with isolines together with 30 gray levels, with dark showing the highest value and bright the lowest.

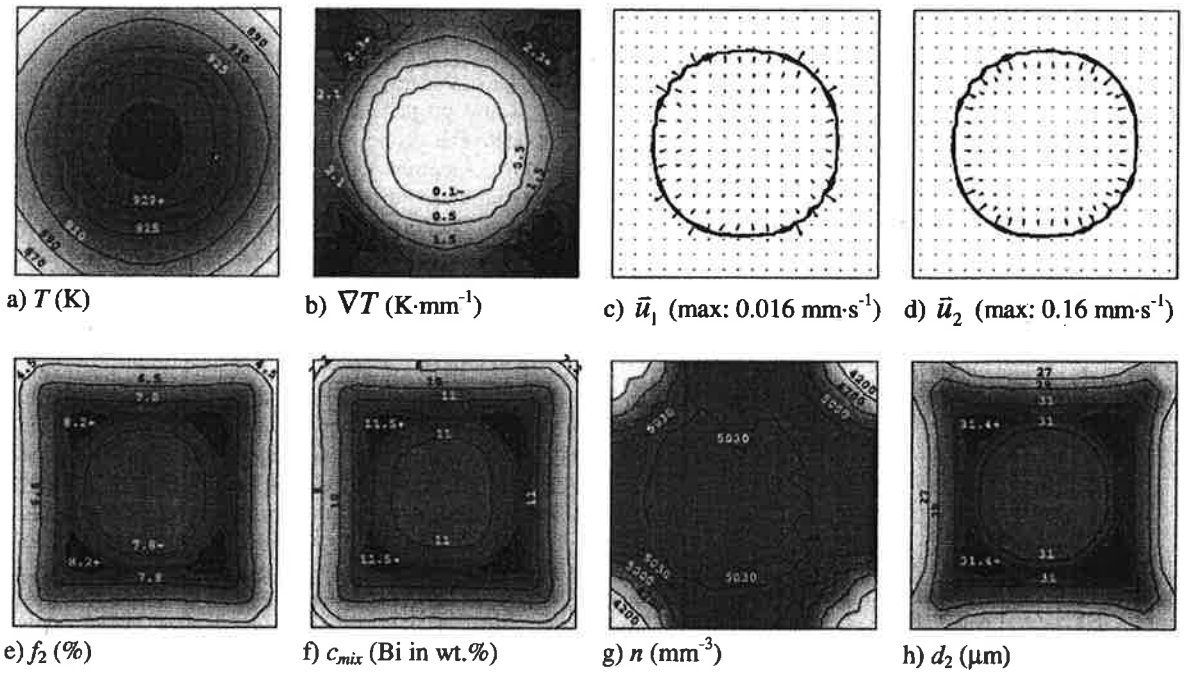

Fig. 6—(*a*) through (*h*) Simulation results at 32.6 s. The arrows of both velocities are linearly scaled from zero to the maximum value given, and the monotectic front (T = 925 K) is drawn together with the velocity fields. All other scalar quantities are shown with isolines together with 30 gray levels, with dark showing the highest value and bright the lowest.

released. The release of the latent heat will reduce the local cooling rate and impact the local temperature gradient ∇T. The "cloverleaf" isolines of ∇T in Figure 5(b) are due to the latent heat of monotectic reaction. The ∇T further influences the Marangoni-induced droplet motion. As shown in Figure 5(d), the maximum velocity of the droplets is no longer in the corners, but near the casting surface where large ∇T is achieved. The velocities of both L_1 and L_2 phases vanish at the corners, when the rigid monotectic matrix (S_A + L_2) forms. Phase separation due to Marangoni-induced droplet motion

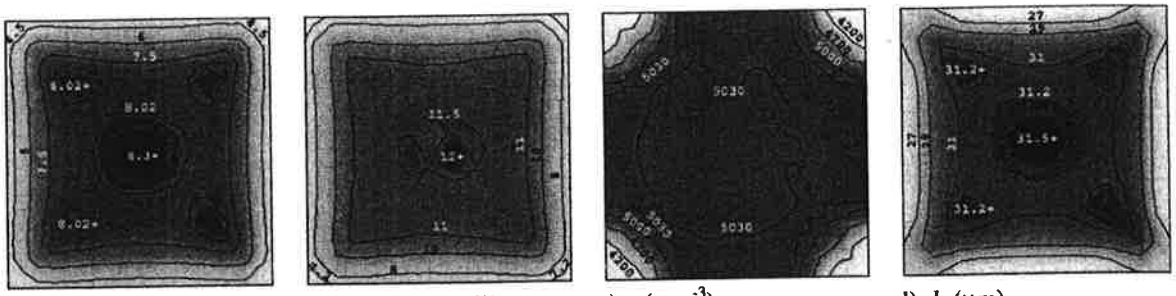

a) f_2 (%) b) c_{mix} (Bi in wt.%) c) n (mm^{-3}) d) d_2 (μm)

Fig. 7—(*a*) through (*d*) The computer-predicted final results. All quantities are shown with isolines together with 30 gray levels, with dark showing the highest value and bright the lowest.

is now obviously seen (Figure 5(e)). The highest volume fraction of the second phase f_2 (>7.6 pct) locates not directly at the corners, but a little far from the corners.

At 32.6 seconds the monotectic front proceeds significantly toward the casting center. The highest velocity (Figures 6(c) and (d)) occurs near the monotectic front. In this stage, the temperature distribution in the casting center (in front of the monotectic front) is quite uniform and the temperature gradient ∇T is smaller than 0.1 K/mm. Behind the monotectic front, especially in the corners, the large temperature gradient ∇T is re-established, but this high ∇T does not influence the phase separation any more. The L_2 droplets behind the monotectic front are already entrapped in the monotectic matrix. Therefore, phase separation occurs only near the monotectic front. Moreover, the maximal velocity of L_2 phase (0.16 mm/s) is much smaller than that in the earlier stage, *e.g.*, the maximal velocity at 3.6 seconds is 0.44 mm/s.

The L_2-phase enriched zones move gradually toward the casting center. The moving speed of L_2 phase is not necessarily equal to the moving speed of the monotectic front. At 15.6 seconds (Figure 5 (e)), four zones of large f_2 locate in front of the monotectic front; at 32.6 seconds (Figure 6(e)), the four zones lie on (nearly behind) the monotectic front, while in the late stage of solidification, the four zones fall behind the monotectic front, and a new L_2-enriched zone forms in the casting center (Figure 7(a)). The moving speed of L_2 phase is governed by the temperature gradient ∇T, and influenced by many factors such as Marangoni coefficient $d\sigma/dT$ and droplet diameter d_2, while the moving speed of the monotectic front is mainly governed by heat transfer. The different moving speeds of L_2 phase and monotectic front are responsible for the final distribution pattern of f_2 in Figure 7(a).

B. *Macrosegregation*

Segregation originates from the solute partitioning during decomposition. In the hypermonotectic alloy (Al-10 wt pct Bi), the solute partitioning during decomposition is strong, *i.e.*, the concentration difference between the decomposed L_2 phase (95.4 to 97.49 wt pct Bi) and the parent melt L_1 (10 to 3.526 wt pct Bi) is very large; so is the segregation tendency. If phase separation occurs, it will definitely cause macrosegregation. The macrosegregation is here quantitatively expressed with a mixture concentration c_{mix}.

As soon as Marangoni-induced droplet motion starts, macrosegregation is immediately detected. At 3.6 seconds, a Bi-enriched segregation zone forms in each corner. Correspondingly, the c_{mix} at the corner and on the surface becomes lower. As time proceeds, the Bi-enriched segregation zone becomes wider and wider, the c_{mix} in the segregation zone becomes higher and higher, and it moves with the motion of L_2 droplet, as shown in Figure 5(f). The final distribution pattern of c_{mix} is similar to that of f_2 (Figure 6(f) and Figure 7(b)). The simulation results further confirm the statement that phase separation is directly responsible for the macrosegregation in hypermonotectic solidification.

C. *Droplet Distribution*

Two processes contribute to the droplet distribution: nucleation and droplet transport by Marangoni-induced droplet motion. The droplet size forms by the diffusion-controlled growth. An empirical heterogeneous nucleation law[18,20,22,23] was implemented in the droplet transport equation as a source term. According to this law, the undercooling $\Delta T = \Delta c/m$ serves as a driving force for the nucleation. The high undercooling (30 K) achieved in the corner and surface regions leads to the high nucleation rate initially. The droplet density n transports following the Marangoni-induced droplet motion of the second phase L_2. The zones with high droplet density (5000 mm^{-3}) in Figure 4(g) are the outcome of the local high nucleation rate and the droplet transport. The favorite cooling condition in the corners is responsible for the local large droplet size shown in Figure 4(h). The droplets grow in the corners to about 25 μm in 3.6 seconds.

At 15.6 seconds, high droplet density n has spread to the whole castings. The droplet density n in the whole casting is relatively uniform. As shown in Figure 5(g), the droplet density in the casting center region is almost equal (5030 mm^{-3}). That is the reason for the asymmetrical isoline of $n = 5030$. In the initial stage, there is a high nucleation rate in the corners, but part of the droplets are transported to the inner region of the casting. In the late stage, the droplets are transported from the outer to the central region, but there is a lower nucleation rate in the casting center. Figure 5(h) shows that the zones with the largest droplets locate in the regions about 13 mm away from the corners. These large droplets are understood to have nucleated near the corner, and then to move gradually toward inner regions. The droplets grow while moving.

In the late stage of solidification, the change of the droplet density distribution is not significant Figures 5 through 7(g). The reasons are as follows. (1) No new droplet nucleates, because the actual ΔT in each element is smaller than ΔT_{max} ever achieved. As explained previously, a new droplet can only nucleate when the actual ΔT exceeds ΔT_{max}. (2) Because the droplet distribution n is relatively uniform, the droplet transport due to Marangoni-induced droplet motion does not change the n distribution significantly. In a given volume element, droplets come in, and almost the same number of droplets move out. The total amount of n in this element remains almost constant. (3) In the late stage of solidification (*e.g.*, Figure 6(d)), Marangoni-induced droplet motion occurs only at the monotectic front, and the maximum $\mathbf{u}_2$ is quite small (~0.16 mm/s).

The final droplet size distribution is shown in Figure 7(d). A tendency of finer droplets on the surface regions (~27 μm) and relatively large droplets in the central casting region (31.5 μm) is predicted. The reasons for this uneven droplet size distribution are Marangoni-induced droplet motion and the diffusion-controlled growth.

D. *Reliable Analyses*

The phase separation phenomenon in hypermonotectic alloys due to Marangoni-induced droplet motion has long since been recognized. The results presented in Figure 7 agree qualitatively well with experiments performed by Walter in sounding rocket experiments using Al-Bi alloys:[30] lower volume fraction of L_2 phase in the boundary regions and higher volume fraction of L_2 phase in the casting center. Nevertheless, it is not possible to compare the modeling results quantitatively with the experiments at this moment. Some reasons are the modeling assumptions, which have been stated in Section II–A. Some other factors, such as the mesh density and the experimental and empirical parameters used for the simulation, also influence the modeling accuracy. They are briefly discussed as follows.

1. Collision and coagulation of the L_2 droplets. The droplet size d_2 increases immediately with coagulation. The d_2 will further influence Marangoni force, hydrodynamic resistance, droplet growth, and mass-transfer rate. Therefore, the collision and coagulation will be necessarily considered in the future models.
2. Mesh density. The relationship between the mesh density and the modeling results has been discussed previously.[18,20] An important criterion for choosing the mesh density is the velocity of the melt convection and the droplet motion. The higher the velocity, the finer the mesh must be. The maximal velocity of the droplet in this system is quite small, *i.e.*, on the order of 10^{-4} m/s. Due to the high calculation cost, the recent simulations were carried out with a grid of 20×20, *i.e.*, the mesh size of 5×5 mm^2 in this casting sample. The authors also performed simulations with coarser (10×10 mm^2) and finer (2.5×2.5 mm^2) meshes by increasing and reducing the casting size. The simulated velocity fields and the distribution profiles of the scalar quantities are similar to the results presented in this article. Therefore, the results presented in this article are representative, and the qualitative statements claimed in this article about the phase separation due to Marangoni motion are reliable. In order to improve the quantitative accuracy, the new computational techniques, *e.g.*, unstructured meshes for the critical regions with sharp gradient and parallel computing for finer mesh, can be taken.
3. Experimental and empirical parameters. For example, a temperature range of 10 K for monotectic reaction is assumed. The latent heat of monotectic reaction is treated to release in the temperature range. It can be predicted that this parameter would influence the temperature distribution, and the temperature distribution would further influence the Marangoni motion. The temperature range for monotectic reaction can be precisely determined experimentally. Other empirical parameters are the nucleation parameters. For equiaxed solidification, according to Rappaz and co-workers,[23,27] the statistic parameters in Eq. [14] can be determined by measuring the grain density (*i.e.*, the grain size) and the corresponding maximum under cooling at recalescence, ΔT_{max}. The same experimental method may not work as well as for the decomposition of L_2 droplets in hypermonotectic alloys. Other experimental methods or alternative nucleation laws[1,28,29] may be necessarily considered.

V. CONCLUSIONS

The newly developed two-phase volume-averaging model is able to simulate the solidification of hypermonotectic alloys including nucleation of the second-phase droplets during decomposition, droplet growth, Marangoni-induced droplet motion, phase separation, monotectic reaction, final droplet distribution, and macrosegregation. The recent model gives a peer insight into the Marangoni-induced droplet motion; the other physical phenomena such as droplet coagulation and gravity-induced sedimentation are excluded from consideration. By analyzing the modeling results for a square casting with a hypermonotectic alloy (Al-10 wt pct Bi) under no-gravity condition, the following findings are obtained.

1. Droplets of the second phase start to nucleate and grow in the corner regions. A large temperature gradient causes the droplets to move toward the inner region by Marangoni-induced droplet motion, and the parent melt moves in the opposite direction.
2. The release of latent heat of the monotectic reaction is found to have a strong impact on the temperature gradient, which further governs the Marangoni-induced droplet motion.
3. The velocity of L_2 phase can be different from the moving speed of the monotectic reaction front. If the monotectic front overtakes the L_2 droplets, the droplets are entrapped in the monotectic matrix, and the velocity of the L_2 phase vanishes.
4. Marangoni-induced droplet motion leads to phase separation. The modeling results show higher L_2 volume fraction in the casting center and lower L_2 volume fraction at the corners.
5. Phase separation is directly responsible for the macrosegregation.
6. Both nucleation and Marangoni-induced droplet motion contribute to the droplet distribution n. In the corners, the nucleation rate is high initially, but part of them move

toward the inner regions. In the late stage, the droplets move to the casting center, but the nucleation rate is low there. Therefore, a relatively uniform n distribution is predicted finally.

7. Marangoni-induced droplet motion and diffusion-controlled growth contribute to the uneven droplet size distribution. A tendency of finer droplets in the surface regions and relatively large droplets in the central region is predicted.

ACKNOWLEDGMENTS

This work was financially supported by the ESA-MAP project "Solidification Morphologies of Monotectic Alloys-MONOPHAS" and the DLR project "Simulation of the Dynamics of Monotectic Solidification." The authors also acknowledge the excellent technical assistance of Drs. Pelzer and Braun, FLUENT (Darmstadt, Germany).

NOMENCLATURE

c_0	alloy concentration
c_c	critical concentration
c_1, c_2	volume-averaged species concentration
c_1^*, c_2^*	interface concentration under thermal equilibrium
Δc_d	$c_2^* - c_1^*$
c_{L2}	L_2 monotectic concentration
c_m	monotectic concentration
c^*	interface species
Δc	$c_1 - c_1^*$
$C_{12}(=-C_{21})$	species exchange rate
$C_{12}^d(=-C_{21}^d)$	species transfer at L_1-L_2 interface
$C_{12}^p(=-C_{21}^p)$	solute partitioning due to phase change
c_{mix}	mix concentration
$c_{p(1)}$, $c_{p(2)}$	specific heat
D_1, D_2	diffusion coefficient
d_2	droplet diameter
f_1, f_2	volume fraction
$\mathbf{f}_M$	Marangoni force on single droplet
$\mathbf{f}_{st}$	Stokes force on a single droplet
$\mathbf{F}_M$	volume-averaged Marangoni force
$\mathbf{g}$	gravity
H	heat-transfer coefficient at casting-mold interface
H^*	volume heat-transfer coefficient between two liquid phases
h_1, h_2	enthalpy
h_1^{ref}, h_2^{ref}	enthalpy at T_{ref}
h^*	interface enthalpy
Δh_d	heat of decomposition
Δh_M	latent heat of monotectic reaction
$K_{21}(=K_{12})$	momentum exchange coefficient
k	solute partitioning coefficient
k_1, k_2	thermal conductivity
L_1, L_2	two liquid phases
M_{12} $(=-M_{21})$	mass-transfer rate per volume
m	slope of liquidus in phase diagram at c_0
m_{12}	mass-transfer rate for a single droplet
N	droplet nucleation rate
n	droplet density
$n_{\max}$	maximum droplet density
p	pressure
$Q_{12}(=-Q_{21})$	energy exchange rate
$Q_{12}^d(=-Q_{21}^d)$	energy exchange by heat transfer
$Q_{12}^p(=-Q_{21}^p)$	energy exchange due to phase change
R	droplet radio
S_A	solid-phase Al
S_B	solid-phase Bi
T_c	critical temperature
T, T_1, T_2	temperature
T_f^A	melting point of pure metal (Al)
T_f^B	melting point of pure metal (Bi)
T_m^f	monotectic temperature
T_{ref}	reference temperature for enthalpy definition
∇T	temperature gradient
ΔT	undercooling
ΔT_N	Gaussian distribution width of droplet nucleation law
ΔT_σ	undercooling for maximum droplet nucleation rate
t	time
$\mathbf{U}_{12}$ $(=-\mathbf{U}_{21})$	momentum exchange rate
$\mathbf{U}_{12}^d$ $(=-\mathbf{U}_{21}^d)$	momentum exchange due to Stokes force
$\mathbf{U}_{12}^p$ $(=-\mathbf{U}_{21}^p)$	momentum exchange due to phase change
u_1, u_2	velocity component in x direction
$\mathbf{u}_1$, $\mathbf{u}_2$	velocity vector
$\mathbf{u}_{12}$, $\mathbf{u}_{21}$	interphase velocity
$\mathbf{u}^*$	interface velocity
v_1, v_2	velocity component in y direction
ρ_1, ρ_2	density
σ	surface tension at liquid-liquid interface
σ_0	experimental parameter in Eq. [19]
$\underline{\mu}_1$, $\underline{\mu}_2$	viscosity
$\underline{\tau}_1$, $\underline{\tau}_2$	stress-strain tensors

Subscripts 1, and 2 indicate first and second liquid phases.

REFERENCES

1. L. Ratke and S. Diefenbach: *Mater. Sci. Eng.*, 1995, vol. 15 (R), pp. 263-347.
2. B. Predel, L. Ratke, and H. Fredriksson: in *Decomposition of Alloys: The Early Stages*, H.U. Walter and M.F. Ashhy, eds., Springer-Verlag, Berlin, 1987, pp. 517-65.
3. B. Prinz, A. Romero, and L. Ratke: *J. Mater. Sci.*, 1995, vol. 30, pp. 4715-19.
4. L. Ratke, G. Korekt, and S. Drees: *Adv. Space Res.*, 1998, vol. 22, pp. 1227-36.
5. L. Ratke and G. Korekt: *Z. Metallkd.*, 2000, vol. 91, pp. 919-27.
6. N.O. Young, J.S. Goldstein, and M.J. Block: *J. Fluid Mech.*, 1959, vol. 6, pp. 350-56.
7. W. Günter: *Über die Dynamik von Fluidpartikeln Aufgrund des Marangoni-Effektes*, VDI-Verlag, Düsseldorf, Germany, 1993, pp. 1-71.
8. M.G. Velarde: in *Materials and Fluids under Low Gravity*, L. Ratke, H. Walter, and B. Feuerbacher eds., Springer-Verlag, Berlin, 1995, pp. 283-98.
9. C. Beckermann and R. Viskanta: *Appl. Mech. Rev.*, 1993, vol. 46, pp. 1-27.
10. J. Ni and C. Beckermann: *Metall. Trans. B*, 1991, vol. 22B, pp. 349-61.
11. C.Y. Wang and C. Beckermann: *Metall. Mater. Trans. A*, 1996, vol. 27A, pp. 2754-64.
12. C.Y. Wang and C. Beckermann: *Metall. Mater. Trans. A*, 1996, vol. 27A, pp. 2765-83.
13. C.Y. Wang and C. Beckermann: *Metall. Mater. Trans. A*, 1996, vol. 27A, pp. 2784-95.
14. C. Beckermann: *JOM*, 1997, vol. 49, pp. 13-17.

15. A.V. Reddy and C. Beckermann: *Metall. Mater. Trans. B*, 1997, vol. 28B, pp. 479-89.
16. J. Ni and F.P. Incropera: *Int. J. Heat Mass Transfer*, 1995, vol. 38, pp. 1271-84.
17. J. Ni and F.P. Incropera: *Int. J. Heat Mass Transfer*, 1995, vol. 38, pp. 1285-96.
18. A. Ludwig and M. Wu: *Metall. Mater. Trans. A*, 2002, vol. 33A, pp. 3673-83.
19. M. Wu and A. Ludwig: *Adv. Eng. Mater.*, 2003, vol. 5, pp. 62-66.
20. M. Wu, A. Ludwig, A. Bührig-Polaczek, M. Fehlbier, and P.R. Sahm: *Int. J. Heat Mass Transfer*, 2003, vol. 46, pp. 2819-32.
21. S. Diefenbach: Ph.D. Thesis, Ruhr-University Bochum, Bochum, Germany, 1993.
22. W. Oldfield: *Trans. ASM*, 1966, vol. 59, pp. 945-61.
23. M. Rappaz: *Int. Mater. Rev.*, 1989, vol. 34, pp. 93-123.
24. F. Falk: in *Immiscible Liquid Metals and Organics*, L. Ratke, ed., DGM Informationsgesellschatt mbH, Oberursel, Germany, 1993, pp. 93-100.
25. S.V. Patankar: *Numerical Heat Transfer and Fluid Flow*, Hemisphere Publishing Corp., Washington, DC, 1980.
26. L. Ratke, S. Dree, S. Diefenbach, B. Pronz, and A. Ahlborn: in *Materials and Fluids under Low Gravity*, L. Ratke, H. Walter, and B. Feuerbacher, eds., Springer-Verlag, Berlin, 1995, pp. 115-33.
27. P. Thevoz, J.L. Desbiolles, and M. Rappaz: *Metall. Trans. A*, 1989, vol. 20A, pp. 311-22.
28. N. Uebber and L. Ratke: *Scripta Metall. Mater.*, 1991, vol. 25, pp. 1133-37.
29. L. Granasy and L. Ratke: *Scripta Metall. Mater.*, 1993, vol. 28, pp. 1329-34.
30. H.U. Walter: *Proc. RIT/ESA/SSC Workshop-ESA SP 219*, Stockholm, Sweden, 1984, Järva Krog, ed., pp. 47-64.